



Relationships between energy release, fuel mass loss, and trace gas and aerosol emissions during laboratory biomass fires

Patrick H. Freeborn,^{1,2} Martin J. Wooster,³ Wei Min Hao,¹ Cecily A. Ryan,¹
Bryce L. Nordgren,¹ Stephen P. Baker,¹ and Charles Ichoku^{4,5}

Received 15 March 2007; revised 20 August 2007; accepted 21 September 2007; published 5 January 2008.

[1] Forty-four small-scale experimental fires were conducted in a combustion chamber to examine the relationship between biomass consumption, smoke production, convective energy release, and middle infrared (MIR) measurements of fire radiative energy (FRE). Fuel bed weights, trace gas and aerosol particle concentrations, stack flow rate and temperature, and concurrent thermal images were collected during laboratory-controlled burns of vegetative fuels. Using two different MIR thermal imaging systems, measurements of FRE taken at polar angles of 48° and 60° were found not to be significantly different from each other ($p < 0.05$), but were significantly different from those obtained at 76° . A simple linear regression revealed that less than 12% of the variation in biomass consumption remained unexplained by the measured FRE regardless of MIR sensor characteristics, fuel type, or viewing angle. Measurements of FRE detected per unit of dry organic material consumed ranged from 1.29 to 4.18 MJ/kg, corresponding to an average of $12 \pm 3\%$ of the higher heating value of the biomass. Whole-fire emission factors agreed with previously reported values, and emission ratios relating total mass production to FRE were determined for CO_2 , CO, NO, NO_2 , and particulate matter less than $2.5 \mu\text{m}$ in aerodynamic diameter. A heat balance performed on the system showed that the release of convective energy could be predicted from a measurement of FRE ($r^2 \geq 0.84$), and together these two modes of heat transfer accounted for $61 \pm 13\%$ of the total, potential heat of combustion available in the preburn solid fuel.

Citation: Freeborn, P. H., M. J. Wooster, W. M. Hao, C. A. Ryan, B. L. Nordgren, S. P. Baker, and C. Ichoku (2008), Relationships between energy release, fuel mass loss, and trace gas and aerosol emissions during laboratory biomass fires, *J. Geophys. Res.*, 113, D01301, doi:10.1029/2007JD008679.

1. Introduction

[2] Although the effects of global biomass burning on tropospheric chemistry and regional air pollution have been qualitatively described [Crutzen and Andreae, 1990], the ability to accurately quantify trace gas and particulate emissions from landscape-scale to regional-scale biomass burning events remains elusive [Hao and Liu, 1994; Andreae and Merlet, 2001]. Several approaches, and several variants of each approach, have been developed in an effort to estimate the amount of biomass consumed as well as the amounts of trace gasses and aerosols injected into the atmosphere [Seiler and Crutzen, 1980; Hao et al., 1990; Kaufman et al., 1990; Ward and Radke, 1993; Hao and Liu,

1994; Scholes et al., 1996a, 1996b]. Each method has inherent advantages and disadvantages, yet the uncertainty associated with each approach is often poorly constrained. To quantify smoke production, most heritage classification methods multiply the area burned by the total fuel consumed per unit area and an emission factor (i.e., mass of trace gas or particulate matter produced per mass of dry fuel consumed). Such emissions estimates are neither spatially nor temporally resolved, but rather represent the total calculated over the duration and extent of the biomass burning event. Furthermore, the development of a new method, or the use of an existing method, is often uniquely dependent on the particular objective of the emission inventory, and the reliability of available information and resources. Options for estimating fuel consumption, for example, range in level of detail from regional default values to the implementation of sophisticated fire behavior models with initial conditions input from experienced land managers [Battye and Battye, 2002]. Though the former is more tractable for continental-scale inventories, the latter allows for more robust characterization of individual fire events. Given that emissions inventories have been performed with differing methodologies, often without overlapping study domains, past and present estimates of

¹Fire Sciences Laboratory, Rocky Mountain Research Station, U.S. Forest Service, Missoula, Montana, USA.

²Now at Department of Geography, King's College London, London, UK.

³Department of Geography, King's College London, London, UK.

⁴Earth Science System Interdisciplinary Center, University of Maryland, College Park, Maryland, USA.

⁵Also at Climate and Radiation Branch, NASA Goddard Space Flight Center, Greenbelt, Maryland, USA.

biomass consumption and trace gas and aerosol production have proved difficult to validate or to compare.

[3] In an effort to construct an alternative method for quantifying trace gas and aerosol production, the relationship between the rate of radiative energy emitted by a fire and the rate of emissions production was first explored by *Kaufman et al.* [1996]. Establishing the total radiative energy emitted by a fire as the standard for measurement, rather than the spectral radiant energy emitted at a particular wavelength, facilitates the division of heat transfer into conduction, convection, and radiation, and allows results to be compared among different sampling platforms. For the Moderate-Resolution Imaging Spectroradiometer (MODIS), *Kaufman et al.* [1998] used multiple simulations of a fire's hypothetical subpixel thermal distribution to derive a constant of proportionality relating the rate of total radiant energy released by the fire to an eighth-order difference between the "fire pixel" and "background pixel" brightness temperatures measured at $3.96 \mu\text{m}$. By approximating Planck's radiation law as a simple power function between the temperature limits found in vegetation fires, *Wooster et al.* [2003] subsequently derived a linear relationship between the rate of total radiant energy release and the excess midwave radiance in the "fire pixel," and also examined the sensitivity of their middle infrared (MIR) radiance method to perturbing factors, including subpixel thermal composition. *Wooster and Zhang* [2004] have further defined the term fire radiative power (FRP) to distinguish the instantaneous units of radiative heat transfer rate (e.g., Watts) from the time-integrated units of energy (e.g., Joules), and it is these definitions of FRP and fire radiative energy (FRE) that are used throughout this work.

[4] Thermal remote sensing of active biomass fires opens two potential pathways for providing spatially and temporally explicit estimates of smoke production. The first pathway, implemented by *Wooster et al.* [2004], uses a measurement of FRE to predict fuel mass loss, then applies a conventional emission factor to calculate the production of trace gases and aerosols. Similar to previous classification methods where the uncertainty of individual components contributed to the overall uncertainty in the estimate [*Taylor and Zimmerman*, 1991], the overall error in smoke production determined in this manner, aside from an error in the measurement of FRE, includes errors associated with the relationship between FRE and mass loss as well as the assumed emission factor. To reduce compounding errors, a second pathway uses a radiative measurement in conjunction with an empirical ratio of smoke emissions to radiative emissions to directly calculate the amount of trace gas and particulate matter produced. The empirical ratio between the mass emission of a trace gas or aerosol to FRE, or FRP, which are also products of combustion, is similar to a traditional emission ratio where the above ambient concentration of a compound of interest is divided by the simultaneously measured above ambient concentration of a reference gas [*Andreae and Merlet*, 2001]. An emission ratio relative to radiant energy is also identical to the emission coefficient proposed by *Ichoku and Kaufman* [2005]. Emission ratios have been calculated relative to reference products of CO_2 or CO depending on whether the compound is primarily emitted during flaming or smoldering combustion, respectively [*Lobert et al.*, 1991]. Similar-

ly, if the radiative component in the denominator is considered the reference product, then accurate estimates of instantaneous smoke emission rates based upon measurements of FRP will depend on the tracking of individual compounds with FRP.

[5] Quantifying biomass consumption and smoke production through a surrogate measurement of FRE, or FRP, requires a well-defined relationship between these two variables. It has been demonstrated that FRE is linearly related to the total amount of fuel consumed, and that FRP and the rate of fuel consumption also show statistically significant relationships with a high degree of linearity [*Wooster*, 2002; *Wooster et al.*, 2005]. Furthermore, *Ichoku and Kaufman* [2005] have developed a series of regional-scale linear relationships between FRP and the mass emission rate of smoke particulate matter, both variables being derived from MODIS observations from the Terra and Aqua satellites.

[6] Since the potential for characterizing emissions production from a time series of FRP has not been fully explored, the following laboratory experiment examines the combustion of a variety of biomass fuels, and includes time-resolved measurements of convective energy release rates, fuel weight loss rates, and trace gas and aerosol emission rates. The influences of different thermal imaging systems, fuel type, and viewing angle on measurements of FRE were also investigated. Measurements of FRE were compared to (1) the total amount of dry organic material consumed and (2) the total mass production of CO_2 , CO, NO, NO_2 , and particulate matter less than $2.5 \mu\text{m}$ in aerodynamic diameter ($\text{PM}_{2.5}$). A temporal analysis of an individual burn was also performed to examine the tracking of instantaneous measurements over time. Fire radiative energy was further compared to the total, potential heat of combustion available in the preburn solid fuel, and also to the total energy liberated in the form of convection. Conclusions are presented with reference to the potential future use of these relationships, and with suggestions for further work.

2. Experimental Methods

2.1. Experimental Design

[7] This experiment was conducted in the U.S. Forest Service's 3600 m^3 combustion facility at the Fire Sciences Laboratory in Missoula, Montana, U.S.A. The arrangement of instruments within the chamber is illustrated in Figure 1, and specifications for each instrument are provided in Table 1. More detailed descriptions of the facility are provided by *Christian et al.* [2003, 2004].

[8] Heterogeneous and homogeneous fuel beds were constructed atop two Mettler Model PM 34 digital scales. Primary fuel samples were collected from unburned forested areas adjacent to the Black Mountain 2 Fire that occurred on the Lolo National Forest in west central Montana during the fire season of 2003 [*Freeborn et al.*, 2004]. Fuel sizes were classified according to the National Fire Danger Rating System [*Burgan*, 1988] and included ponderosa pine (*Pinus ponderosa* Dougl. ex Laws.) needles less than 0.635 cm in diameter, Douglas fir (*Pseudotsuga menziesii* (Mirb.) Franco) twigs between 0.635 cm and 2.54 cm in diameter, ponderosa pine branches between 2.54 cm and 7.62 cm in

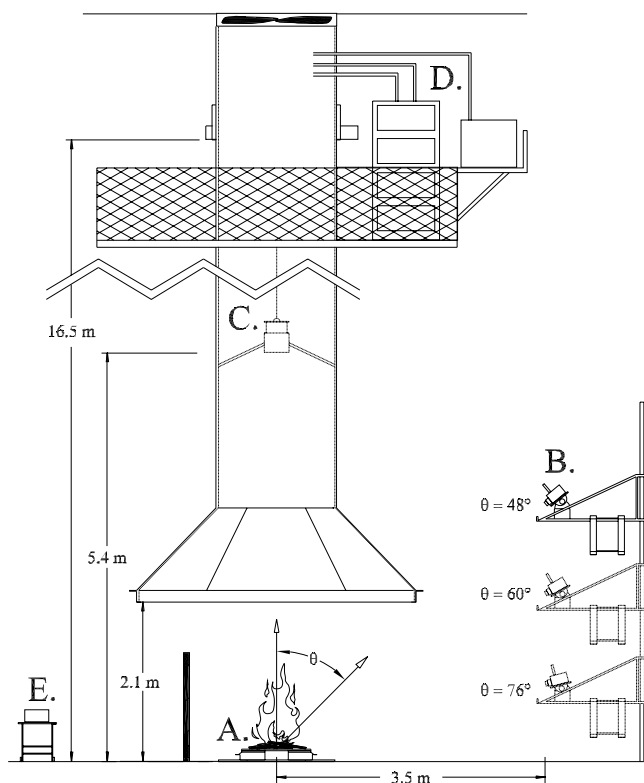


Figure 1. Combustion chamber sampling arrangement. See Table 1 for specifications of instruments at locations A through E.

diameter, and live herbaceous and woody Douglas fir foliage. Other fuels included senesced grass collected from Zambian dambos, shredded aspen (*Populus* spp.) in the form of excelsior, big sagebrush (*Artemisia tridentata* Nutt.), and western white pine needles (*Pinus monticola* Dougl. ex D. Don) [Burns and Honkala, 1990]. Fuels were arranged in horizontal piles to facilitate ignition, but in some cases a wire mesh and sand substrate were used to position

the dambo grass vertically in order to better simulate the arrangement of natural vegetation at the end of the dry season.

[9] A subset of the fuel was weighed and placed in a drying oven at 37°C for 24 h; after which it was reweighed, and fuel moisture content was calculated on a dry-weight basis. The total mass of water within each heterogeneous fuel bed was determined based upon individual fuel moisture contents and the fractional contribution of individual fuel components to the total bed mass. It was assumed that all water, free, bound, and produced during combustion, exited the combustion zone as superheated vapor and condensed upstream of the stack temperature measurement. Condensation of water on the remaining char and ash after the fires extinguished was considered negligible in the final mass loss measurement.

[10] One thermal imaging system, a CMC Electronics Cincinnati TVS-8500 ($\sim 3.4\text{--}5.1\ \mu\text{m}$), was cantilevered at the end of a vertical rail to provide oblique observations at three fixed polar angles (θ) of 48° , 60° , and 76° . The imager was set to assume a target emissivity of unity, and a black plate was positioned behind the fire to prevent specular reflections from metallic objects otherwise in the scene. Nadir-looking observations were obtained with a narrowband AGEMA-550 thermal imager ($\sim 3.9\ \mu\text{m}$), previously used in the experiments of Wooster *et al.* [2005]. The AGEMA-550 was mounted inside a pressurized canister with a germanium window and suspended within the sampling stack approximately 5.4 m above ground level. The AGEMA-550 was also set to assume a target emissivity of unity. Each imager was first calibrated against a Mikron Infrared Inc. M300 blackbody source, and though repeatedly exposed to smoke during the experiment, the transmissivity, τ , of the germanium window remained constant ($\tau = 0.93$). A sensor-to-sensor cross calibration was also performed by observing ten fires from collocated positions at the zenith, and at polar angles of 48° , 60° , and 76° . Since it was not possible to install both imagers in the stack, collocated measurements at the zenith were taken from the 16.5 m sampling platform shown in Figure 1. Atmospheric attenuation primarily due to CO_2 and H_2O absorption was

Table 1. Location and Specifications of Instruments Used in the Combustion Chamber (See Corresponding Schematic in Figure 1)

Location	Instrument	Specifications
A	Mettler Model PM34 Digital Scale	fine range: 4.0 kg with 0.1 g readability; coarse range: 32.0 kg with 1.0 g readability
B	CMC Electronics Cincinnati Model TVS-8500 Thermal Imager	3.4–5.1 μm “twin peaks” spectral response; 256 \times 236 InSb focal plane array; 1 mrad spatial resolution (IFOV); accuracy of $\pm 2\%$ or $\pm 2^\circ\text{C}$; 14 bit file format
C	AGEMA-550 Thermal Imager	3.9 μm “flame filter” spectral band; 320 \times 240 PtSi focal plane array; 1.1 mrad spatial resolution (IFOV); accuracy of $\pm 2\%$ of range or $\pm 2^\circ\text{C}$; 12 bit file format
D	Thermo Environmental Instruments Model 48C CO Analyzer	detection: gas filter correlation (GFC); variable range: 0–1 up to 0–1000 ppm; precision: $\pm 1\%$ full scale or ± 0.02 ppm
D	TSI Model 3563 Nephelometer	integrating nephelometer ($7\text{--}170^\circ$); peak wavelengths at 700, 550, and 450 nm; response time < 10 s
D	Thermo Environmental Model 42 NO, NO ₂ , NO _x Analyzer	detection: chemiluminescence; range: 0 to 2000 ppb, ± 0.5 ppb; 40 s rise and fall time over 10 s average
D and E	Li-Cor Model Li-6262 CO ₂ /H ₂ O Analyzer	detection: NDIR gas analyzer; CO ₂ range to 1000 ppm, ± 1 ppm at 350 ppm; H ₂ O range: 0 to 74 mB, 1% of reading

considered negligible over the short sensor-to-target distances and low relative humidities measured in the combustion chamber [Fuss and Hamins, 2002].

[11] Concentrations of NO and NO₂ were measured with a Thermo Environmental Model 42 chemiluminescent NO_x analyzer. Measurements of stack CO and CO₂ were taken, respectively, with a Thermo Environmental Instruments, Inc., Model 48C and a Li-Cor, Inc., Model Li-6262. High- and low-level CO and CO₂ calibrations were performed prior to each burn. A second CO₂ sensor, stationed at floor level away from the fire, measured fluctuations in the background due to diffusion and human respiration. Modified combustion efficiencies (MCE) for flaming and smoldering phases were calculated as the ratio of CO₂ to the sum of CO₂ and CO [Ward and Radke, 1993]. Rather than separating combustion phases at maxima in the CO production rate [Lobert et al., 1991], predominantly flaming and smoldering processes were instead subjectively determined from video recordings so as to more closely coincide with conventional ground sampling techniques implemented underneath Fire Atmosphere Sampling System (FASS) towers [Susott et al., 1990; Babbitt et al., 1996; Hao et al., 1996].

[12] The total mass of PM_{2.5} emitted over the duration of the fire was determined by filtration and gravimetric analysis. Real-time PM_{2.5} concentrations were obtained by temporally integrating the scattering coefficient (550 nm) measured with a TSI Model 3563 Nephelometer, and calibrating this value to the mass of PM_{2.5} collected during filtration. Retrieval of instantaneous PM_{2.5} mass emission rates in this manner assumed a constant ratio between the scattering coefficient and mass concentration throughout the lifetime of the fire. Although the mass scattering efficiency has been found to vary because of changes in particle size, morphology, and refractive index [Chen et al., 2006], the application here of a constant value yielded a general profile of instantaneous PM_{2.5} emission rates that, while presumably distorted in magnitude, permitted the inspection of the onset and duration of fire behavior events. All comparisons and statistical analyses relevant to total PM_{2.5} emissions were performed using gravimetric measurements, not the optical retrievals.

[13] Average stack air temperatures were measured with two chromel-alumel thermocouples. Instantaneous mass flow rates were calculated by multiplying trace gas and PM_{2.5} concentrations by the cross sectional area of the stack (1.82 m²) and the fluid velocity measured by a Kurz Model 455 hot-wire anemometer. Assuming standard air as the working fluid, instantaneous release rates of convective energy were calculated using the total mass flow rate in the stack, a constant pressure specific heat, and the temperature difference between the stack flow and the chamber ambient.

[14] All stack sampling instruments, including the digital balances, were interfaced to a multichannel data logger with a sampling frequency of 0.5 Hz. Both thermal imagers had a sampling frequency of 1 Hz, and were synchronized to each other as well as to the multichannel data logger. Timestamps associated with the measurements of stack concentrations were shifted by the time required for a parcel to travel the stack distance, and also by the lag times attributed to plumbing distances, flow rates, and instrument response.

2.2. Image Processing Chain and FRE Algorithm

[15] All measurements of FRP for this experiment were calculated via the MIR radiance method of Wooster et al. [2003], which has been previously applied to imagery collected from ground-based and satellite-based platforms [Wooster et al., 2004, 2005; Roberts et al., 2005]. Wooster et al. [2005] include a detailed sensitivity analysis of this approach which requires the determination of the MIR spectral radiance on a per pixel basis. Thermal imagers deliver measurements of pixel brightness temperature, and since the band-pass filter of the AGEMA-550 is essentially monochromatic at 3.9 μm, the Planck function was used to calculate pixel-level spectral radiance measures for this instrument, L_{AGEMA} (W m⁻² μm⁻¹ sr⁻¹). A direct substitution of blackbody temperature and wavelength into the Planck function cannot be used to retrieve radiance values for the TVS-8500 since this imager is sensitive to radiation within a spectral band, rather than a discrete wavelength. To eliminate molecular band radiation due to CO₂ emission centered at approximately 4.3 μm, the TVS-8500 has a “twin peaks” spectral response, $R_{TVS}(\lambda)$, composed of two imperfect rectangular functions. Therefore the mean spectral radiance, or the band-pass radiance, for the TVS-8500, L_{TVS} (W m⁻² μm⁻¹ sr⁻¹), was calculated by numerically integrating the following equation at 0.01 μm intervals:

$$L_{TVS} = \frac{\int_{3.4\mu\text{m}}^{5.1\mu\text{m}} L(\lambda, T) R_{TVS}(\lambda) d\lambda}{\int_{3.4\mu\text{m}}^{5.1\mu\text{m}} R_{TVS}(\lambda) d\lambda} \quad (1)$$

where $L(\lambda, T)$ is the spectral radiance calculated from the Planck function. Using equation (1), a temperature to band-pass radiance look up table (LUT) was generated at a resolution of 0.5 K, and linear interpolations were performed to retrieve values at sub-0.5 K precision.

[16] Sequences of thermal images were analyzed according to the processing chain and computational algorithm presented in Figure 2. First, an absolute minimum detection threshold was applied to every pixel in the image. A pixel was considered to contain fire if the spectral or band-pass radiance exceeded 57.6 W m⁻² μm⁻¹ sr⁻¹ (477 K), or 186.4 W m⁻² μm⁻¹ sr⁻¹ (553 K), for the AGEMA-550 or TVS-8500, respectively. These criteria were established based solely upon detector sensitivity and thus background noise at the bottom of each imager’s temperature range setting.

[17] Within an image, i , the instantaneous fire radiative power, FRP_i , and fire area, A_i , were calculated such that:

$$FRP_i = \frac{A_{\text{sampl}} \sigma}{a} \sum_{f=1}^{n_f} (L_f - L_{bg}) \quad (2)$$

$$A_i = n_f A_{\text{sampl}} \quad (3)$$

where A_{sampl} is the area of an individual ground cell being sampled, $\sigma = 5.669 \times 10^{-8}$ W m⁻² K⁻⁴ is Stefan-Boltzmann’s constant, a is a power law coefficient determined according to the MIR radiance method [Wooster

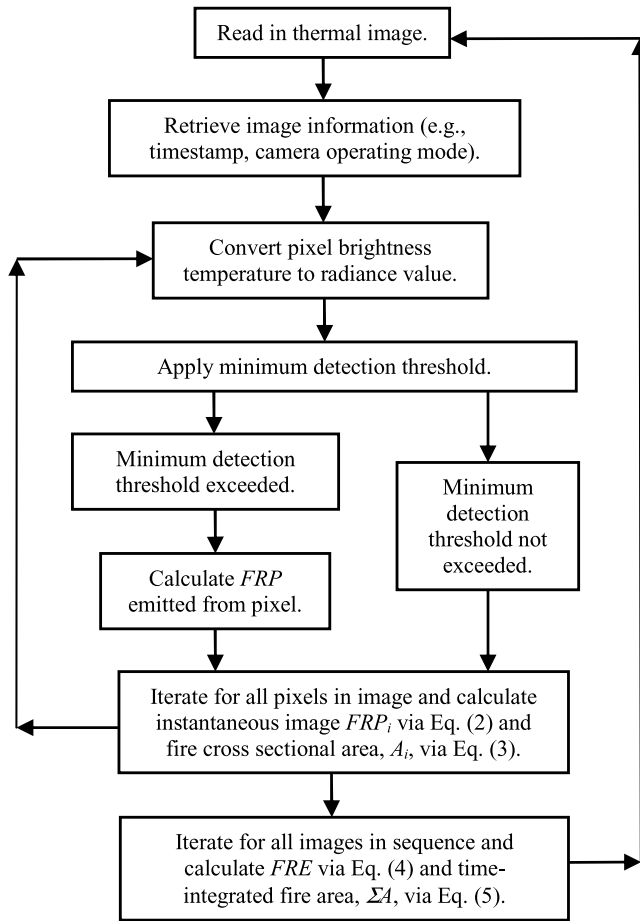


Figure 2. Flowchart of the thermal image processing chain.

et al., 2003], n_f is the number of pixels per image that exceed the minimum detection threshold (i.e., the number of “fire pixels”), L_f is the radiance measurement for an individual fire pixel, and L_{bg} is the background radiance contribution from within the fire pixel. The power law coefficients, a , for the TVS-8500 and the AGEMA-550 were 2.45×10^{-9} and $2.93 \times 10^{-9} \text{ W m}^{-2} \mu\text{m}^{-1} \text{ sr}^{-1} \text{ K}^{-4}$, respectively. Equation (2) is a direct application of the MIR radiance method [Wooster *et al.*, 2003], and is the approach previously reported by Wooster *et al.* [2005]. Both equations (2) and (3) are generalized expressions that are further tailored to the specific imager and viewing geometry when implemented in the algorithm. In this work, the specific imager that measured FRP and fire area will be identified by the subscripts “AGEMA” or “TVS.”

[18] Both the background radiance, obtained from a separate measurement of the chamber ambient temperature, and A_{sampl} were held constant over the entire image. This viewing geometry assumed that the fire image plane was oriented parallel to the focal plane array (FPA), and individual detectors subtended equivalent areas. With this configuration there was no difference in angle between the normal of the focal plane and the normal of the image representation of the fire. This two dimensional over simplification not only eliminated the need for 3D registration, but was fundamentally analogous to the classical planar

representation of a blackbody and allowed radiant heat transfer to be treated as an interaction between two solid surfaces.

[19] Fire radiative energy and time-integrated fire area, ΣA , measured by each sensor were calculated by numerically integrating the temporal profiles of FRP and fire area:

$$FRE_{sensor} = \sum_{i=1}^{n_i} FRP_i \Delta t_i \quad (4)$$

$$\Sigma A_{sensor} = \sum_{i=1}^{n_i} A_i \Delta t_i \quad (5)$$

where *sensor* identifies the particular imager that performed the measurement, n_i is the number of images in the sequence, and Δt_i is the sampling interval between successive images, not the actual dwell time of the sensor. Since the summations in equations (4) and (5) treat temporal profiles as step functions, it must be assumed that the fire’s radiative properties and geometry behaved as rectangular pulses having widths equal to the sampling interval.

3. Results and Discussion

3.1. Summary of the Data Set

[20] In total, 44 individual burns were analyzed (i.e., sample size $n_b = 44$). Thirty-one fires were simultaneously observed with two thermal imaging systems, ten of which were observed from collocated positions, and 35 fires had complimentary mass loss measurements. Ambient temperatures at the floor of the chamber ranged from 21°C to 29°C, and relative humidities at the platform ranged from 6% to 11%. Initial fuel bed masses ranged from 0.20 kg to 2.90 kg, including fuel moisture content. Dead fuel moisture contents had a mean of 7.1% ($\pm 1.3\%$), and the live moisture content of one sample of *Psme* foliage was measured at 44.8%. Durations ranged from approximately 6 minutes to 2.5 h, and total organic mass loss ranged from 0.17 kg to 2.51 kg. Flaming processes had a mean MCE of 0.98 (± 0.01), while smoldering processes had a mean MCE of 0.89 (± 0.04), which agreed well with results of previous laboratory studies [Yokelson *et al.*, 1996; Goode *et al.*, 1999].

3.2. Sensor-to-Sensor Comparisons of Measured FRE and Fire Area

[21] To eliminate the confounding effects of different thermal imagers and different line-of-sight distance measurements that were not taken from a hemisphere, ratios of collocated measurements of FRE and time integrated fire area were categorized by the polar angle of the observation. For collocated measurements obtained at zenith, the mean ratio of FRE_{AGEMA} to FRE_{TVS} was 0.81 ± 0.01 ($n_b = 3$), while the mean ratio of ΣA_{AGEMA} to ΣA_{TVS} was 1.59 ± 0.11 ($n_b = 3$). Although based on a small sample size, a comparison of collocated measurements revealed that mean ratios of FRE and time integrated fire area at 48° ($n_b = 2$), 60° ($n_b = 2$), and 76° ($n_b = 3$) were each significantly different ($p < 0.05$) than the mean ratios obtained at zenith. These results suggest that collocated ratios are dependent upon the polar angle of the observation.

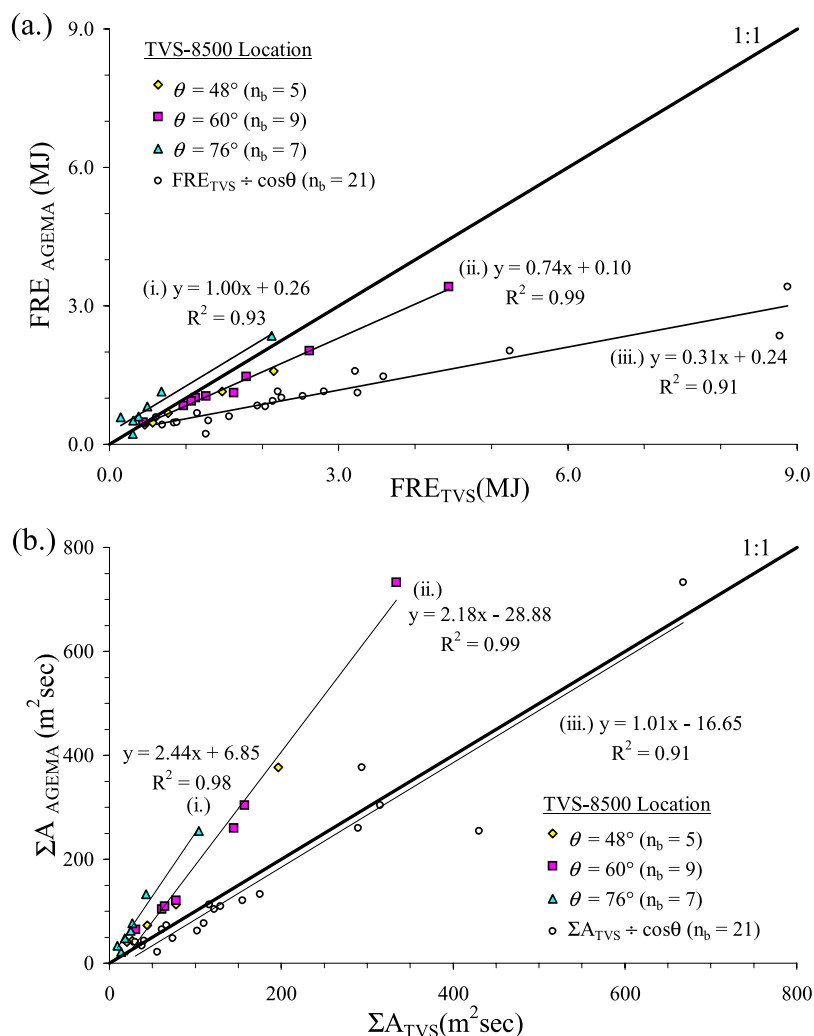


Figure 3. Comparisons between nadir and off-nadir measurements of (a) FRE and (b) time-integrated fire area. The three linear regressions correspond to relationships between measurements taken with the AGEMA-550 at the zenith and measurements taken with the TVS-8500 at polar angles of 76° (line i), 48° and 60° (line ii), and 48° , 60° and 76° (line iii) corrected by the cosine of the polar angle.

[22] Sensor-to-sensor comparisons were also conducted to ascertain the influence of viewing angle, fuel type, and MCE when predicting a nadir-looking measurement of FRE from an off-nadir measurement (Figure 3). Here the AGEMA-550 remained fixed at the zenith, while the TVS-8500 was positioned at an oblique viewing angle. A linear regression analysis of 21 burns was performed, and the following regression results were drawn on the basis of p values and F tests with a tolerable probability of a Type I error (α) specified at 0.05: (1) Even though viewing angle and fuel type were variables having geometric manifestations, interaction between these two terms was not significant. (2) The inclusion of either MCE or fuel type by themselves added no further predictive value to the regression. (3) For FRE, slopes and intercepts at 48° and 60° were homogeneous, but significantly different from those at 76° . (4) For time-integrated fire area, the slopes of the regression lines were homogeneous regardless of viewing angle, however the intercept at 48° and 60° was significantly different from that at 76° . These results indicate that radiometric measure-

ments taken at polar angles of 48° and 60° could not be distinguished from each other, but were statistically different from those obtained at 76° .

[23] For sensor-to-sensor comparisons here, and only here, supplementary calculations were performed by orienting the fire image plane parallel to the fuel bed. With this orientation, the fire image remained registered to the center of the fuel bed, and the difference in angle between the vector normal of the fire image and the vector normal of the focal plane was the polar angle of the observation. Since the area of the focal plane array and the instantaneous area of the fire were relatively small compared to the square of the separation distance, measurements of time-integrated fire area and FRE were divided by the cosine of the polar angle (Figure 3). All future results of FRP and FRE are presented based upon actual measurements, and are not corrected for the observation angle.

[24] Sensor-to-sensor differences between instantaneous measurements of FRP, and thus FRE, were inherent since the AGEMA-550 and the TVS-8500 have unique spectral

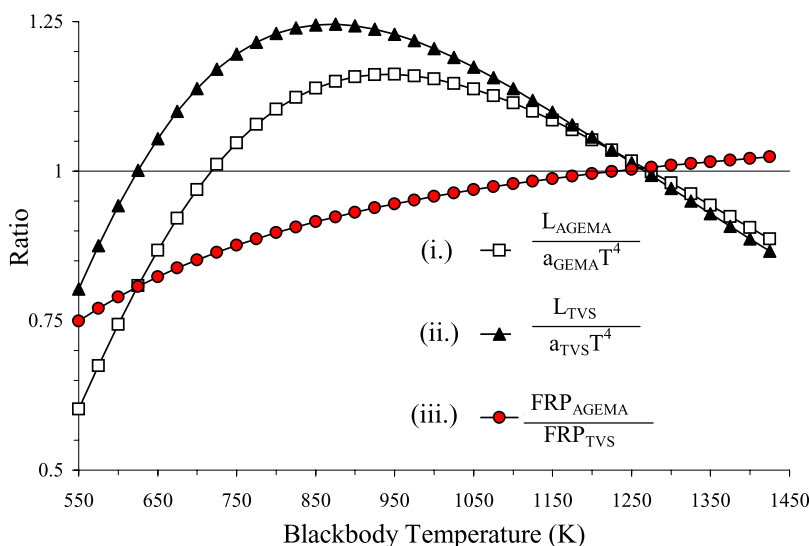


Figure 4. As a function of blackbody temperature, the ratio of AGEMA-550 spectral radiance to the radiance predicted by the best fit power law (line i), the ratio of TVS-8500 band-pass radiance to the radiance predicted by the best fit power law (line ii), and the theoretical ratio of FRP measured with the AGEMA-550 to that measured by the TVS-8500 (line iii).

response functions. If the imagers had the same instantaneous field of view (IFOV), and observed the same blackbody target, then the theoretical ratio of FRP_{AGEMA} to FRP_{TVS} derived from a sensor specific expression of equation (2) would be the product of two ratios: namely the temperature-dependent ratio of L_{AGEMA} to L_{TVS} multiplied by the constant ratio of a_{TVS} to a_{AGEMA} (Figure 4). Since pixelated ratios of FRP were temperature-dependent, concurrent and collocated image ratios of FRP were affected by the fire's instantaneous thermal distribution (Figure 5). The “scene-integrated” effective brightness temperature of the fire, T_{eff} , measured by the TVS-8500 is also presented in Figure 5 and was calculated by summing band-pass radiance values weighted by their fractional area, then backing out the brightness temperature from the LUT.

[25] Differences in FRP simultaneously measured by the AGEMA-550 and the TVS-8500 were also attributed to differences in measured fire area (Figure 5), and thus differences in sensor optics and absolute fire detection criteria. The IFOV of the detector affects measurements of brightness temperature since different subpixel thermal distributions will be subtended, and images taken with a lower spatial resolution will represent the fire's two-dimensional cross section more coarsely. Furthermore, the effect of the minimum “fire pixel” detection threshold (477 K for the AGEMA-550 and 553 K for the TVS-8500) on measured fire area at this scale is most consequential at the following locations: (1) along the exterior perimeter of a flame envelope where entrained air dilutes the reactants and products of combustion; (2) at holes within the flame

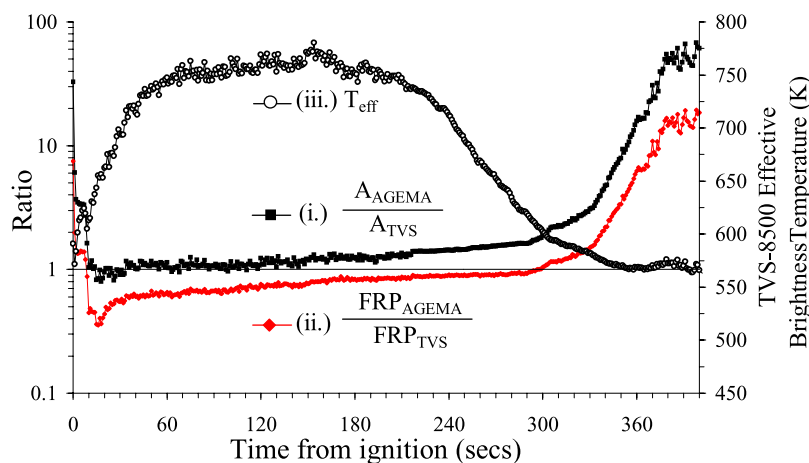


Figure 5. Instantaneous image to image ratios of fire area (line i) and FRP (line ii) measured by the two different thermal imagers from collocated positions at 48° . Also scaled to the right axis is the effective brightness temperature, T_{eff} , measured by the TVS-8500 (line iii).

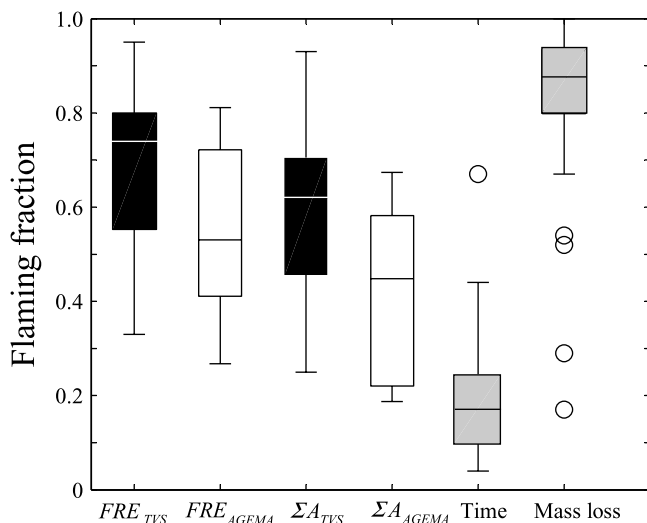


Figure 6. Fractions of fire radiative energy, time-integrated fire area, fire duration (time), and mass loss contributed by the flaming stage of combustion. Measurements for the TVS-8500 are presented without regard to observation angle, and measurements for the AGEMA-550 were always taken from the zenith. Circular markers indicate outliers and extreme values.

envelope, due to turbulence or an optically thin path length; and (3) on exposed surfaces of the solid fuel where the reaction zone is either propagating or decaying. Therefore, with the full fire in each imager's field of view, differences in measured fire area were attributed to boundary approximations, either geometric because of a pixilated representation of a free form surface, or radiometric because of thresholds based upon the strength of a thermal signal. It is for these reasons, in general, that collocated measurements were angularly dependent, and it is for these reasons, specifically, that despite the decrease in effective fire temperature after flame quenching, the ratio of FRP_{AGEMA} to FRP_{TV5} continued to increase (Figure 5).

3.3. Temporal Characteristics of Biomass Combustion

[26] To summarize the temporal nature for all fires conducted during this experiment, fractional contributions of FRE, time-integrated fire area, duration, and total mass loss were separated by combustion phase (Figure 6). Whereas flaming fractions (p_f) of FRE and time-integrated fire area included contributions from the flame as well from the fuel bed, smoldering fractions ($1 - p_f$) were generally limited to contributions from the fuel bed alone. During the flaming phase, rays traced from a detector to an individual fuel component passed through the flame, therefore it cannot be stated whether or not more FRE per unit area was emitted from the exposed solid fuel surface or from the flame. Though flaming phases existed for considerably shorter durations, fractions of time-integrated fire area were more balanced because of the considerably larger instantaneous fire areas present during flaming than during smoldering. Also, since the TVS-8500 observed a greater number of small, quick fires (where the AGEMA was not used), the mean value of FRE_{TV5} was slightly inflated. For only the fires observed with both thermal imaging systems, a mean

flaming fraction of 0.64 for FRE_{TV5} is more appropriately compared to 0.55 for FRE_{AGEMA} . Such differences in FRE are coupled to differences in ΣA since at oblique viewing angles the TVS-8500 observed a greater cross section of the flame, but less of the fuel bed.

[27] A normalized temporal profile of an individual burn during which 0.56 kg of dambo grass was consumed illustrates the typical tracking of FRP with mass loss rate, convective energy release rate, and trace gas and $PM_{2.5}$ emission rates (Figure 7). The fuel mass loss rate in Figure 7 also includes the mass loss of water associated with the moisture content. To aid in the interpretation, instantaneous ratios of mass loss rate, CO_2 emission rate, and CO emission rate with respect to FRP are presented in Figure 7b. The form of the scatterplots (Figure 7c) agree with previous comparisons between instantaneous emission ratios of NO_x (nitrogen oxides) and CH_3CN (acetonitrile) relative to CO_2 and CO [Lobert *et al.*, 1991]. Individual point measurements are identified by combustion phase (open circles and black diamonds represent flaming and smoldering, respectively) and follow sequentially; the origin represents ignition as well as extinction. The three linear regressions relating FRP to either CO_2 or CO emissions rate in Figure 7c are fit to (1) all of the measurements; (2) measurements collected during the flaming stage until the peak mass emission rate for CO_2 , or FRP for CO; and (3) measurements collected only during the smoldering stage. The peak in CO_2 emission rate occurred at 84 s, the peak in FRP occurred at 123 s, and the peak in CO emission rate occurred at 222 s after ignition.

[28] Several events accentuate the uniqueness of biomass combustion, as well as the sensitivity and utility of measurements of FRP. Upon ignition, gas phase combustion above the fuel bed generated the initial buoyant flux most noticeable in the convective and CO_2 emission profiles. Likewise, the upward force induced by the buoyant parcel, and sensed by the digital scales was responsible for the cluster of flaming measurements uncharacteristically below the linear regression relating instantaneous mass loss rate and FRP_{TV5} (Figure 7c). During the first 12 s the heating element used to ignite the fuel bed dominated radiative emission. Afterward, until peaks in CO_2 emission rate and FRP, instantaneous emission ratios of CO_2 and CO relative to FRP were fairly constant at 1586 ± 263 and $4.18 \pm 0.74 \text{ g s}^{-1}/\text{MW}$, respectively. In the time between these two peak events and the complete cessation of flaming, the emission ratio of CO_2 relative to FRP continued to decrease while the emission ratio of CO continued to increase. Contrary to our abrupt, visual distinction of fire behavior, this phenomenon is attributed to the gradual transition from predominantly flaming to smoldering areas that existed simultaneously within the fuel bed, and is substantiated by a continual decrease in MCE from 0.99 at ignition to a local minimum of 0.89 at 230 s.

[29] At 200 s, all initial flames were extinguished, and at approximately 240 s, a detached flame reignited above the fuel surface. This event appeared as a local spike in FRP, and was further evidenced by an increase in CO_2 production, and a dramatic decrease in CO production, due to increased reaction rates and more complete combustion within the flame envelope. The decrease in the emission ratio of CO production rate relative to FRP at 240 s (Figure

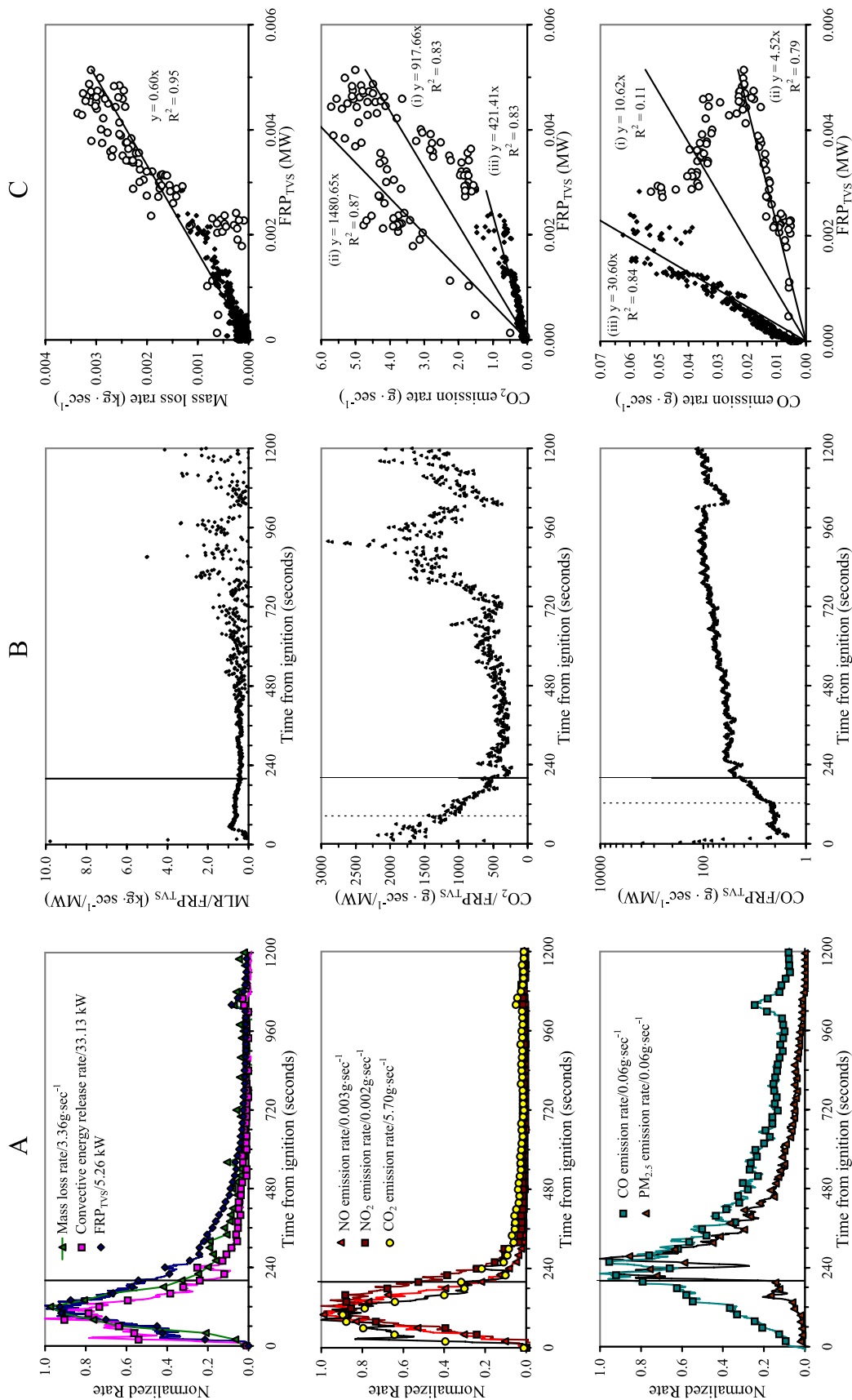


Figure 7. (a) Normalized profiles of FRP, mass loss rate, convective heat transfer rate, and trace gas and aerosol emission rates classified into primarily flaming and smoldering compounds. (b) Instantaneous ratios and (c) instantaneous comparisons for mass loss rate, CO₂ and CO emission rate with respect to FRP. The solid lines in Figures 7a and 7b represent the cessation of flaming. The dotted lines in Figure 7b represent peaks in CO₂ emission rate and FRP which were used to separate linear regressions in Figure 7c. In Figure 7c, the open circles and black diamonds represent flaming and smoldering respectively.

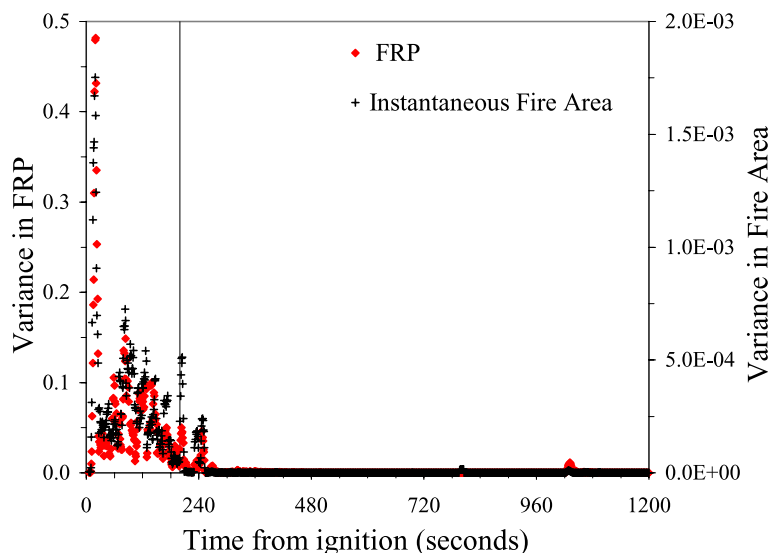


Figure 8. For the burn presented in Figure 7, the variance calculated over a moving 10-s window for FRP (red diamonds) and instantaneous fire area (black crosses) as measured with the TVS-8500. Both flare-ups at 240 and 1040 s are evident.

7b) indicates that the rate of CO production decreased compared to the rate of radiant energy released, and is analogous to the smaller emission factors for CO at higher combustion efficiencies [Ward and Hardy, 1991], and higher fire intensities [Sandberg, 1974]. A simultaneous perturbation at 240 s was not detected in the mass loss rate, nor in NO_x source strengths, because of noise induced by turbulent air currents, and the relatively slow response of the analyzers, respectively.

[30] The increase in the ratio of CO₂ emission rate with respect to FRP beginning at 720 s (Figure 7b) is due to the increased production of CO₂ during a prolonged combustion event not detected by the thermal imaging system. Here combustion reactions occurred deep within the fuel bed such that the optical depth of the fuel complex prevented thermal radiance from reaching the sensor. At approximately 900 s, however, the combustion front reached the surface of the fuel bed and radiant energy was eventually measured.

[31] A second local peak in FRP occurred at 1040 s as the combustion front encountered a preheated, predried pocket of exposed fuel. Here, both instantaneous ratios of CO and CO₂ emission rate relative to FRP decreased while a flamelet was sustained for approximately 12 s. In contrast to the event at 240 s, the absolute production rate of CO at 1040 s actually increased, suggesting a difference in combustion mechanisms. At 1040 s, the flamelet was weak, very brief, and overwhelmed by the relatively large, hot surface area of glowing combustion within the fuel bed. Thus the increased radiometric signal dominated the increase in either CO or CO₂ production, and both instantaneous emission ratios relative to FRP decreased because of an inversely proportional relationship with FRP. Furthermore, measurements of FRP were presumably underestimated during the smoldering phase as some fire pixels fell beneath the minimum detection threshold, and emitter temperatures of cooling material fell below the domain of applicability (~650 K)

for the MIR radiance method. Therefore, as previously cool pixels during smoldering combustion became hot during glowing combustion, the net change in FRP calculated at 1040 s using the MIR radiance algorithm was presumably greater than the true increase in the fire's radiative power and contributed to the universal decrease in instantaneous emission ratios relative to FRP.

[32] The temporal resolution and coverage achieved during this experiment allowed variances in FRP and fire area to be calculated over a moving 10-s window (Figure 8). Variances in both measurements were much greater during flaming than smoldering, especially when measured from oblique viewing angles. Such fluctuations were also noticed during in situ measurements of crown fire activity [Butler *et al.*, 2004]. Greater variance here is attributed to (1) relatively rapid changes in flame geometry due to turbulence; (2) relatively rapid changes in kinetic temperatures within the flame, and on surfaces of the solid fuel, due to temporal differences chemical reaction rates; and (3) relatively rapid changes in measured brightness temperatures due to differences in gas and vapor composition, soot concentration, particle size distribution, and ultimately, emissivity. After flames extinguished, however, thermal emission was less variable in time since solid-state reactions on fuel surfaces during smoldering were considerably less dynamic than (1) gas-phase reactions occurring within the flame envelope and (2) solid-state reactions on fuel surfaces that were influenced by feedback interactions with the flame.

3.4. Relationships Between Total Biomass Consumption and FRE

[33] For each burn, measurements of FRE were compared to the total amount of dry organic material consumed (Figure 9). Ratios of FRE measured by the AGEMA to total mass loss ranged from 1.29 to 4.18 MJ/kg ($n_b = 18$). Although it appears at first contradictory, relationships

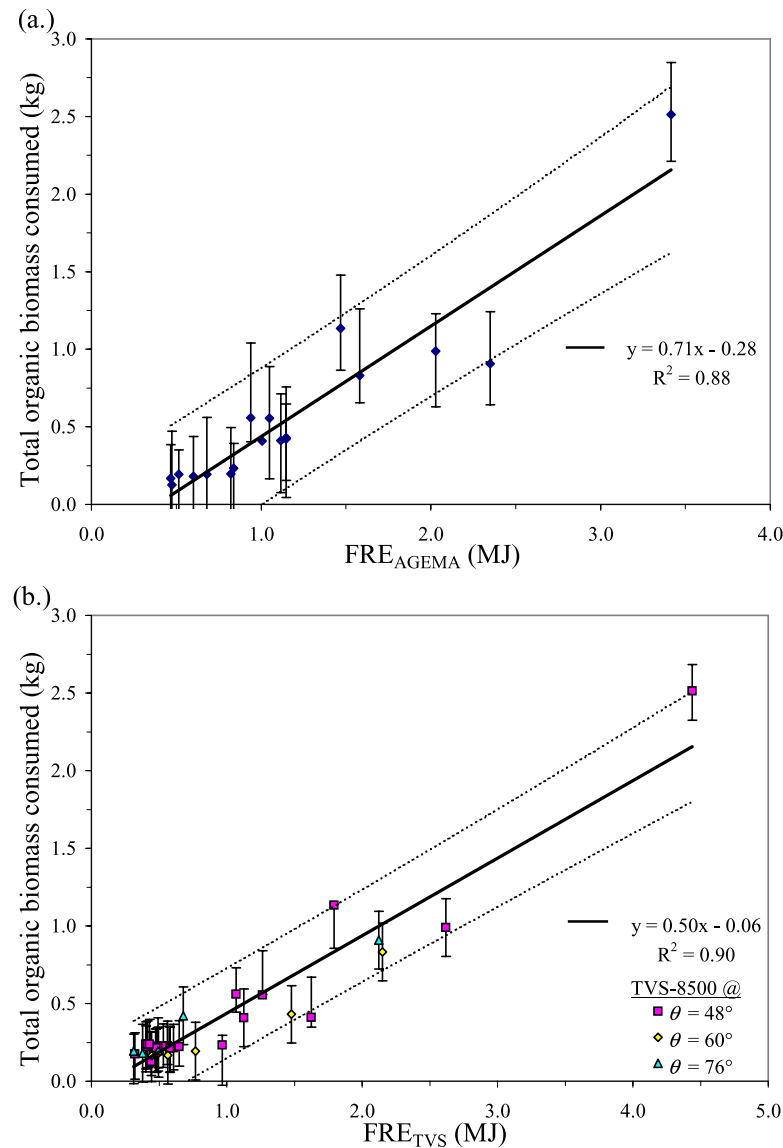


Figure 9. Linear regressions relating total biomass consumption to FRE measured by (a) the AGEMA always located at the zenith and (b) the TVS-8500 located at polar angles of 48° , 60° , and 76° . The solid lines depict a simple linear regression, the dashed lines depict a 95% individual prediction interval for a simple linear regression, and the error bars depict a 95% individual prediction interval for a full multiple regression with all significant variables included in the model.

between FRE and fuel mass loss are presented here in two different units: the slope of the linear regression is expressed in kg/MJ since FRE would be the independent variable used to predict fuel consumption, whereas individual ratios are expressed as MJ/kg to more closely resemble the units of a traditional emission factor and the heat of combustion (i.e., the amount of energy released as heat per unit of fuel consumed during complete combustion). Nevertheless, a multiple regression analysis revealed that MCE added no further power when predicting total fuel mass loss from FRE, but fuel type was significant at the $\alpha = 0.05$ level. Although including fuel type as an explanatory variable raised the coefficient of determination (r^2) from 0.88 to 0.98, and decreased the standard error from 0.20 kg to 0.12 kg, six independent variables were also added such that the

model accounted for seven of the 17 total degrees of freedom. If knowledge of fuel type is unavailable, however, a simple linear regression may suffice since less than 12% of the variation in total biomass consumption remains unexplained by the amount of fire radiative energy measured with the nadir-viewing AGEMA-550.

[34] The observation at which 2.51 kg of biomass was consumed is a high leverage point. After removing this data point, the effect of fuel type on the relationship between FRE and total fuel mass loss was found to be not significant, and forcing the intercept through the origin yielded a slope of 0.453 kg/MJ with a 95% confidence interval of ± 0.068 kg/MJ. This slope nearly overlaps that of 0.368 ± 0.015 kg/MJ reported previously for *Miscanthus* grass by Wooster *et al.* [2005]. Since the high leverage point is

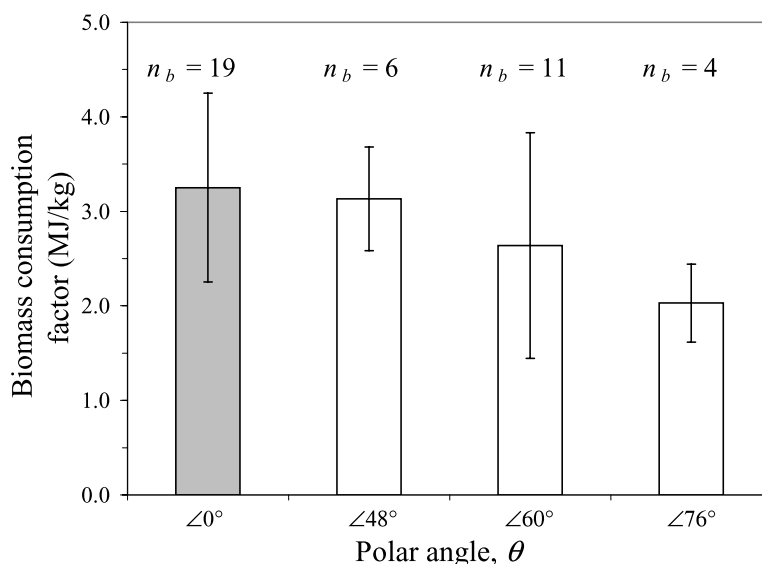


Figure 10. Mean ratio of FRE to total mass loss categorized by polar angle. Radiative measurements at 48° , 60° , and 76° were taken with the TVS-8500. Radiative measurements at the zenith were taken with the AGEMA-550 and were corrected by the ratio of FRE_{AGEMA} to FRE_{TVS} determined during the collocated sensor-to-sensor cross calibration.

included in, and does not distract from, the sensor-to-sensor cross calibration (Figure 3), the radiometric observation is considered genuine.

[35] Ratios of FRE_{TVS} to the total amount of dry biomass consumed ranged from 1.58 to 4.13 MJ/kg ($n_b = 35$). A simple linear regression neglected viewing angle, fuel type, and their interaction (Figure 9). A multiple regression analysis found that interaction between viewing angle and fuel type was significant, and viewing angle and fuel type separately added further predictive power at the $\alpha = 0.05$ level. After removing two data points associated with the combustion of live vegetation, however, fuel type was found to be not significant. This suggests that either the chemical composition associated with the phenology of *Psme* foliage, the moisture content, the combustion characteristics, or a combination of all three influenced this relationship.

[36] The effect of viewing angle was further investigated by comparing mean ratios of FRE to total mass loss classified by the polar angle of the observation (Figure 10). To eliminate the confounding effects of different imagers, nadir-looking measurements taken with the AGEMA-550 were corrected by the time-integrated ratio of FRE_{AGEMA} to FRE_{TVS} determined from the nadir-looking, collocated, cross calibration detailed in section 3.2. On average, less energy was detected per unit of fuel consumed as the viewing angle became more oblique. As the polar angle increased there was (1) an increase in measured fire area during flaming due to the exposed sheet of flame; (2) a decrease in path length through the flames, and hence shallower optical depths and lower emissivities as chords of line-of-sight rotated through flame heights to flame widths; and (3) a decrease in measured fire area during smoldering due to the decreased exposure of the fuel bed. Figure 10 also demonstrates that fuel type induced enough variation to overwhelm any angular effects possibly incurred at 48° , and especially at 60° which also included

the only two measurements of live fuels. Nevertheless, if viewing angle and fuel type are ignored, less than 10% of the variation in total biomass consumption remains unexplained by the amount of fire radiative energy measured with the TVS-8500.

3.5. Direct Relationships Between Trace Gases, Aerosols, FRE, and FRP

[37] Simple and multiple regressions relating FRE to total CO_2 and CO production are presented in Figure 11. For the AGEMA-550, the full model includes fuel type, and for the TVS-8500, the full model includes fuel type and viewing angle, but again multiple regressions accounted for nearly half the degrees of freedom. Unlike the relationship between FRE and fuel mass loss, however, if fuel type and viewing angle were ignored, the inclusion of MCE added further predictive power. These results suggest that although MCE by itself was significant when predicting CO_2 and CO production from a measurement of FRE, as might be expected since CO and CO_2 emission factors depend strongly on combustion process and thus MCE [Ward and Hardy, 1991], knowledge of fuel type and viewing angle is more important.

[38] To corroborate current measurements with those of previous experiments, whole-fire emission factors were determined by dividing the total amount of a product species emitted by the total amount of biomass consumed (Table 2). The mean and standard deviation of the emission factors were categorized by the type of fuel bed, and agree reasonably well with those obtained under similar experimental designs [Yokelson *et al.*, 1996; Goode *et al.*, 1999]. Unlike previous measurements, the total mass of fuel consumed in this experiment was determined using preburn and postburn readings of the digital scales rather than the carbon mass balance (CMB) method of Nelson [1982] in order to provide independent observations of fuel consumption and trace gas production. Based upon the relatively

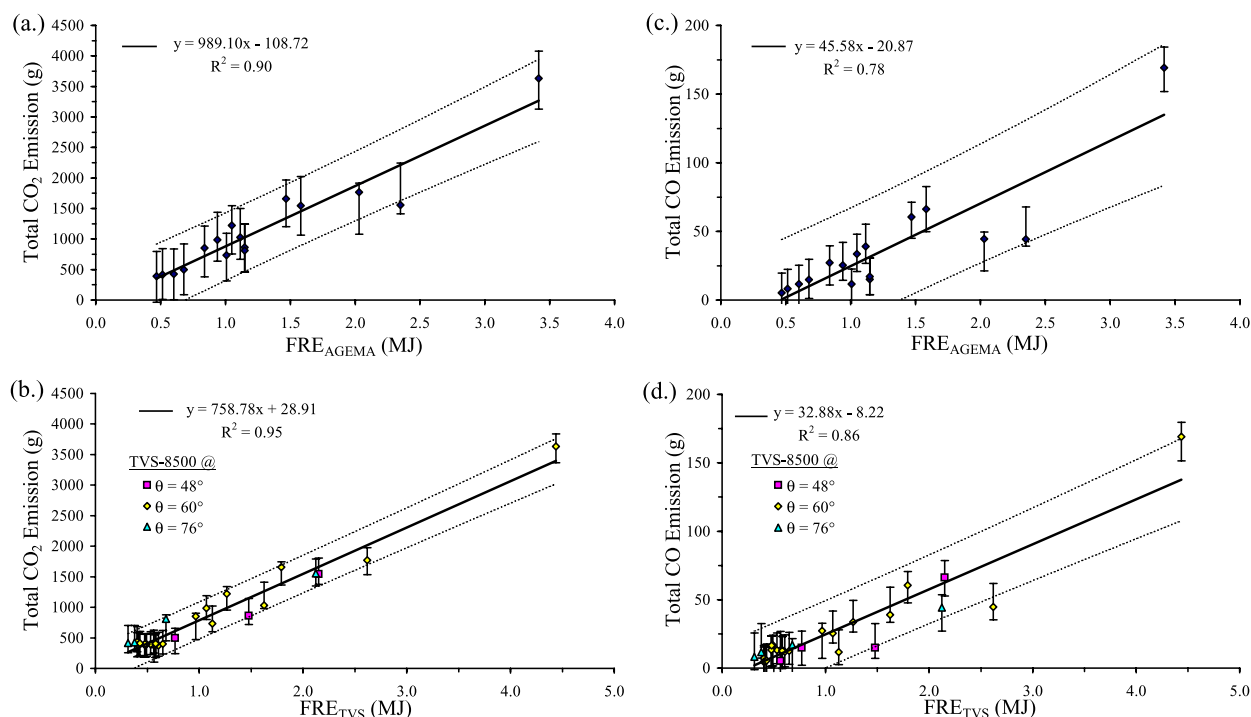


Figure 11. Relationships between FRE measured by each thermal imager and total mass production of (a and b) CO_2 and (c and d) CO . Solid lines depict a simple linear regression, the dashed lines depict a 95% individual prediction interval for the simple linear regression, and the error bars depict a 95% individual prediction interval for a full multiple regression with all significant variables included in the model.

accurate replication of previously published emission factors, corresponding emission ratios relative to FRE were developed by dividing total emissions production, on a mass basis, by FRE (Table 2).

[39] Neither the average of instantaneous emission ratios calculated over the duration of the burn (see Figure 7b), nor the slope of the regression line about the instantaneous emission rates (see Figure 7c), is comparable to the time-integrated ratio of total emissions production to FRE (see Table 2). The average of the instantaneous emission ratios is strongly influenced by the number of observations, and hence the duration of the smoldering phase. Therefore, in the past, whole fire emission ratios were developed by weighting instantaneous emission ratios by the mass of fuel consumed over the interval the sample was collected [Andreae and Merlet, 2001]. Weighted averages were not calculated for this experiment due to noise in the mass loss profile and the presumably overestimated instantaneous emission ratios relative to FRP obtained during smoldering.

[40] Since the method of least squares attempts to minimize residuals, linear regressions performed on flaming compounds generally passed through nearly contemporaneous peaks in emissions rate and FRP (see Figure 7c). Thus the slopes of the regressions about instantaneous values, for example FRP versus CO_2 emission rate, were more representative of flaming combustion, and were 19% ($\sigma = 12\%$, $n_b = 18$) greater than time-integrated, whole-fire emission ratios. Both the slopes about instantaneous measurements, and the whole-fire emission ratios, were in turn bracketed by relationships between emissions production rate and FRP

during predominantly flaming processes immediately after ignition and smoldering process well into the burn.

[41] Nearly simultaneous peaks in FRP and CO_2 production rate occurred when the fuel bed was nearly fully involved, and gaseous combustion above the fuel bed was at a volumetric maximum. At this time there was the greatest, absolute rate of conversion of carbon to CO_2 , as well as the greatest opportunity for CO , emitted as a result of incomplete combustion at the edge of the fuel bed, to be swept into the flames and completely oxidized. Likewise, brightness temperatures associated with solid-state combustion on the surfaces of fuel particles, and the combined cross sectional area of the glowing fuel bed and the flame envelope, were at a maximum thereby producing a peak in the radiometric signal. Two different values of CO_2 emission rate, however, exist on either side of this peak for a given value of FRP depending on the time the measurement was taken during the combustion process. This relationship reinforces the work of Yokelson *et al.* [1996] which describes the simultaneous occurrence and sequential transition of flaming, smoldering, and pyrolysis reactions as the fire front propagates and decays across a fuel bed. After ignition, and before flames extinguished, effluents were composed of products emitted from a combination of combustion processes that were spatially distributed within the entire reaction zone. Furthermore, baffles in the stack also mixed products emitted within a temporal window estimated to be as wide as 5 s. Once the flames extinguished, however, emissions production was dominated by relatively homogeneous smoldering processes. Meas-

Table 2. Whole-Fire Emission Factors and Radiative Emission Ratios Relative to FRE

Fuel Description	CO ₂ /FRE Emission Ratio, g/MJ		CO/FRE Emission Ratio, g/MJ		NO/FRE Emission Ratio, g/MJ		NO ₂ /FRE Emission Ratio, g/MJ		PM _{2.5} /FRE Emission Ratio, g/MJ			
	CO ₂ Emission Factor, g/kg	TVS- 8500	AGEMA 550	CO Emission Factor, g/kg	TVS- 8500	AGEMA 550	NO ₂ Emission Factor, g/kg	TVS- 8500	AGEMA 550	PM _{2.5} Emission Factor, g/kg	TVS- 8500	AGEMA 550
Mean	2234.42	1012.19	821.85	37.04	17.88	13.69	PIPO ^a (1 h) ^b	1.41	0.95	1.13	0.48	0.41
Standard deviation	128.83	454.89	14.89	7.48	11.96	3.29	2.93	0.93	0.22	0.30	0.12	0.09
n _b	(2)	(2)	(2)	(2)	(2)	(2)	0.57	(2)	(2)	(2)	(2)	(2)
Mean	1906.32	809.07	728.37	34.64	15.22	13.18	1.68	0.72	1.59	1.17	0.48	0.45
Standard deviation	103.93	333.30	22.87	5.95	8.59	1.62	0.24	0.33	0.29	0.15	0.13	0.07
n _b	(3)	(3)	(3)	(3)	(3)	(3)	PSME (10 h)	(3)	(3)	(3)	(3)	(3)
Mean	1752.47	704.5	767.22	46.95	18.95	20.41	0.99	0.39	2.48	1.25	0.50	0.55
Standard deviation	52.47	40.89	147.95	2.65	2.73	2.19	0.25	0.07	1.02	0.15	0.02	0.15
n _b	(2)	(2)	(2)	(2)	(2)	(2)	PIPO (1 h), PSME (10 h), PIPO (100 h)	(2)	(2)	(2)	(2)	(2)
Mean	1843.27	988.08	1210.44	51.61	27.93	37.48	1.09	0.60	1.84	0.76	0.41	0.45
Standard deviation	284.93	95.25	197.74	13.99	8.20	9.94	0.49	0.29	0.50	0.22	0.14	0.14
n _b	(5)	(5)	(4)	(5)	(5)	(4)	Dambo grass (1 h)	(5)	(4)	(5)	(5)	(4)
Mean	3074.33	758.29	971.02	105.48	26.07	33.71	2.94	0.72	1.09	1.75	0.43	0.55
Standard deviation	806.85	175.82	67.33	15.02	2.90	1.79	0.95	0.21	0.14	0.42	0.09	0.03
n _b	(2)	(2)	(2)	(2)	(2)	(2)	PIPO (1 h), PSME foliage (live)	(2)	(2)	(2)	(2)	(2)
Mean	1764.85	923.54	976.41	35.91	16.83	41.88	0.83	0.45	3.90	0.55	0.21	0.29
Standard deviation	111.05	153.08	na	10.80	9.34	na	0.23	0.18	na	na	na	na
n _b	(4)	(4)	(1)	(4)	(4)	(1)	Populus ssp. (1 h)	(4)	(1)	(1)	(1)	(1)
Mean	1956.33	813.63	722.08	67.39	28.33	20.58	3.74	1.58	0.90	0.60	0.25	0.37
Standard deviation	325.45	141.03	16.85	8.02	5.49	0.27	0.20	0.29	0.05	0.43	0.19	0.11
n _b	(8)	(8)	(2)	(8)	(8)	(2)	ARTR2 foliage and stems	(8)	(2)	(8)	(8)	(2)
Mean	1808.03	652.26	nd	57.49	20.74	nd	PIPO3 (1 h)	1.05	nd	0.68	0.25	nd
Standard deviation	70.90	44.97	nd	2.01	1.48	nd	2.90	0.11	nd	0.15	0.06	nd
n _b	(4)	(4)	nd	(4)	(4)	nd	0.19	(4)	nd	(4)	(4)	nd
Grand mean	1943.02	823.99	877.58	55.12	22.93	25.51	2.30	0.96	1.68	0.87	0.35	0.45
Grand standard deviation	424.92	185.43	157.84	22.01	8.01	11.93	1.22	0.54	0.87	0.44	0.17	0.12
n _b	30	30	16	30	30	16	30	30	16	27	16	15

^aPIPO: *Pinus ponderosa* Dougl. ex Laws., PSME: *Pseudotsuga menziesii* (Mirb.) Franco, ARTR2: *Artemisia tridentata* Nutt., PIPO3: *Pinus monticola* Dougl. ex D. Don.

^bFuel Size Class per the National Fire Danger Rating System (NFDERS), 1 h <0.635 cm diameter, 0.635 cm diameter <10 h <2.54 cm diameter, and 2.54 cm diameter <100 h <7.62 cm diameter.

urements before and after the peak also differed to the extent that thermal emission from still cooling ash and char contributed to FRP [Wooster *et al.*, 2005], but not to smoke production.

[42] Smoldering products of combustion tracked relatively well with CO emissions, but not with FRP. Linear regressions fit to instantaneous measurements of smoldering products generally passed between temporally different maxima in emission rate and radiative power output. The time between the different maxima represents the transition from predominantly flaming to predominantly smoldering processes. Again the slopes of the regression lines relating CO emission rates to FRP were influenced by flaming measurements, however for smoldering compounds this served to reduce the value of the best fit slope. Here values for the slopes about instantaneous measurements of CO emission rate and FRP were 34% ($\sigma = 20\%$, $n_b = 18$) less than the time-integrated ratio of total mass production of CO to FRE. Again these relationships were bound by the maximum and minimum emission ratios obtained during smoldering, and during the initial stages of flaming, respectively. Although instantaneous relationships between CO emission rate and FRP were not linearly correlated during the lifetime of a burn, temporal profiles for both these products of combustion exhibited the same general form, though shifted in time. Thus total CO production and FRE were proportional to each other, and linear regressions between these two had relatively high correlation coefficients. Ultimately the correlation between FRE and total CO was much stronger than that between instantaneous emission rates, but still not as strong as the correlation between FRE and the total yield of CO₂ since CO₂ is also a product preferentially emitted during flaming combustion.

3.6. Radiant and Convective Fractions

[43] The radiant fraction, χ_r , is the fraction of total energy liberated in the form of radiation during the combustion process. Heats of combustion, or higher heating values (HHV), have been extensively studied for forest fuels using bomb calorimetry and evolved gas analysis [Susott *et al.*, 1979; Susott, 1982a]. For this experiment, heats of combustion ranged from 17.9 to 22.5 MJ/kg, and were referenced based upon species and part of foliage, or where data was unavailable, values were calculated from equations relating the heat of combustion to the measured carbon content of the fuel [Susott *et al.*, 1975; Klass, 1998]. Based upon total organic mass loss, and the HHV, which assumes complete combustion, radiant fractions were calculated with respect to the potential thermal energy available in the preburn solid fuel. Radiant fractions for the nadir-looking AGEMA had an average of $12.4 \pm 3.4\%$ ($n_b = 18$). These values were similar to an average of $12.1 \pm 3.0\%$ ($n_b = 35$) for the TVS-8500 regardless of viewing angle. Radiant fractions for this experiment agreed well with an average of $11.7 \pm 2.4\%$, using the gross heating content for *Miscanthus* grass fuels, as performed by Wooster *et al.* [2005], but are less than an average of 17% for wood crib fires, as performed by Fons [1946] and cited by Brown and Davis [1973].

[44] Also calculated with respect to the HHV of the biomass, a mean convective fraction of $51.8 \pm 9.0\%$ ($n_b = 35$) was determined by integrating the convective profile

over time. Note that calculations using the HHV included the latent heat released during condensation of the product water vapor, and that the elevated stack temperature used to calculate convective energy release was also due in part to this phase change. A simple linear regression analysis indicated that the total convective energy generated throughout the lifetime of a fire could be predicted from a measurement of FRE taken with either the AGEMA-550 ($r^2 = 0.84$) or the TVS-8500 ($r^2 = 0.87$). Although the ratio of FRE to convective energy measured during this experiment is approximately one quarter of that previously measured during the combustion of wooden cribs [McCarter and Broideo, 1965], comparisons are limited since the cribs were suspended above the ground and radiative fluxes were integrated over a sphere rather than a hemisphere.

[45] A heat balance performed on the system demonstrated that convective energy plus FRE measured with either the AGEMA-550, or the TVS-8500, accounted for $62 \pm 13\%$, or $64 \pm 10\%$, respectively, of the total heat of combustion of the biomass. The remainder of the heat was balanced by (1) conduction; (2) the energy required to mechanically drive and also evaporate moisture from the fuel; (3) the endothermic energy required to raise the fuel to ignition temperature, and to initiate self-sustaining chemical reactions [Susott, 1982b]; and (4) the differences in the heat of combustion between volatiles and char [Susott, 1982a]. Of the compounds of incomplete combustion only CO was measured to account for $2.3 \pm 1.3\%$ ($n_b = 35$) of the potential heat of combustion. Acknowledging the unmeasured energy losses in the system, the total energy measured during this experiment strongly agrees with the suggestion that the effective heat of wood is approximately 65% of the HHV obtained in an oxygen bomb [White and Dietenberger, 1999].

4. Conclusions and Suggestion for Future Work

[46] For a range of different fuel types found in key fire-affected temperate and tropical ecosystems, we have made the first laboratory-controlled, contemporaneous measurements of four of the key fire parameters, namely biomass consumption, trace gas and particulate matter production and FRE. Results from this study agree fully with those of Wooster [2002] and Wooster *et al.* [2005] in that total mass loss, and mass loss rate, during a burn were found to be linearly proportional to FRE, and FRP, respectively. Coefficients of the relationships were weakly dependent upon dead and senesced fuel type and polar angles less than $\angle 60^\circ$, but were strongly influenced by live vegetation and extreme viewing geometries. We have also extended previous efforts by directly examining both instantaneous and total emissions production, and comparing these to, respectively, fire radiative power and energy. Though total CO₂ and CO production were found proportional to FRE, instantaneous emission ratios relative to FRP were dependent on the evolutionary stage of the fire, most particularly for those species preferentially emitted during smoldering combustion. Since ratios between total smoke production and total fuel mass loss agreed with previously reported emission factors, and energy balances performed on the system agreed with previous calculations, emission ratios of total emissions production relative to FRE are considered valid.

As with previous experiments conducted in a laboratory environment, the emission ratios presented here are more representative of fires with higher combustion efficiencies than those generally experienced on the landscape. Although only a few product species were measured, relationships developed here can be cross-referenced to previously reported emission factors [Andreae and Merlet, 2001], and could be used in conjunction with midwave thermal infrared imagery to estimate the atmospheric injection of more specific compounds.

[47] Future laboratory experiments should more closely examine the tracking of emission rates with FRP in order to develop temporally dependent relationships, and to better relate instantaneous and time-integrated emission ratios with respect to FRP and FRE. It is also suggested that the emissions patterns presented in Figure 7c be compared across different fuel types and fire sizes, and that the transition between predominantly flaming and smoldering phases be characterized, perhaps using temporal variations in FRP and fire area to discriminate combustion processes.

[48] For time-integrated values, the synthesis of laboratory relationships and field data assumes a direct, linear extrapolation beyond measurements collected during this study. Therefore it is recommended that future experiments be conducted in a field environment to (1) extend the range of empirical data; (2) test the hypothesis of linearity; and (3) determine if the division of heat transfer, or at least the measurement thereof, remains constant regardless of the size and intensity of the fire. Estimates of the total amount of fuel consumed within small plots (i.e., ~ 0.1 acre) located in forested ecosystems could be obtained through preburn and postburn inventories [Brown, 1974], however fire behavior and fuel consumption models would be more appropriate for simulating first-order fire effects for larger study sites observed with a thermal imaging system. Though coupling relationships from this laboratory experiment with satellite data can be used to project emissions, these results should be used more appropriately to enhance the analysis of thermal imagery collected from ground-based [Freeborn et al., 2004, 2006] and airborne platforms, and to facilitate a ground-upward approach to calibrating and validating satellite imagery.

[49] In a field setting the thermal radiance detected via remote sensing is perhaps the only product of combustion that can, in theory, be measured over the entire area of the fire. As evidenced in section 3.3, however, fuel consumption and emissions production cannot be estimated if thermal radiance emitted by the fire never reaches the sensor. Obstructions such as canopy cover in forested ecosystems, or topography in high relief terrain, can attenuate or even completely obscure the thermal signal thereby underestimating fuel consumption and emissions production. The effect of such obstructions, as well as attenuation by the atmosphere and smoke plumes, on localized relationships between fuel consumption, emissions production, and radiative energy should be investigated. Furthermore, diurnal fluctuations of fire spread and intensity must also be considered if infrequent thermal infrared observations are to be used to estimate total fuel consumption and emissions production over the entire duration of a fire.

[50] As with previous whole-fire emission factors and emission ratios, the application of empirical relationships

relative to FRE must be considered with respect to the temporal and spatial resolution of the field observation. The application of time-integrated relationships to instantaneous estimates will ultimately underpredict CO₂ production rates during predominantly flaming combustion, overpredict CO₂ production rates during predominantly smoldering combustion, and conversely affect simultaneous predictions for CO production rates. Although laboratory experiments offer an opportunity to derive emission ratios relative to FRP for “purely flaming” or “purely smoldering” combustion phases, their eventual application necessarily requires the ability to distinguish individual combustion processes at the landscape level. Therefore it is strongly recommended that future work address, perhaps through simulations, the influence of subpixel combustion composition, instantaneous emission rates, and thermal distribution on agglomerated, whole-pixel relationships between FRP and source strength.

[51] **Acknowledgments.** The authors would like to thank Emily Lincoln of the Fire Science Laboratory for assisting with the trace gas and aerosol measurements. We would also like to thank Gareth Roberts of King's College London for developing the software tools necessary to process the thermal images collected with the AGEMA-550. Martin Wooster's involvement in this study was supported by NERC grants NERC/NE/C520712/1 and NERC/Z/S/2001/01027.

References

- Andreae, M. O., and P. Merlet (2001), Emission of trace gases and aerosols from biomass burning, *Global Biogeochem. Cycles.*, *15*(4), 955–966.
- Babbitt, R. E., D. E. Ward, R. A. Susott, P. Artaxo, and J. B. Kauffman (1996), A comparison of concurrent airborne and ground-based emissions generated from biomass burning in the Amazon basin, in *Proceedings of SCAR-B: Smoke-Sulfate, Clouds, and Radiation-Brasil*, edited by V. Kirchhoff, pp. 23–26, Transtec Editorial, Sao Jose dos Campos, Brazil.
- Battye, W., and R. Battye (2002), Development of emissions inventory methods for wildland fire, *EPA Contract 68-D-98-046*, Off. of Air Qual. Plann. and Stand., U. S. Environ. Prot. Agency, Research Triangle Park, N. C. (Available at <http://www.epa.gov/ttn/chief/ap42/ch13/related/fire-rept.pdf>)
- Brown, A. A., and K. P. Davis (1973), *Forest Fire: Control and Use*, 686 pp., edited by W. P. Orr, N. Frankel, and S. Langman, McGraw-Hill, New York.
- Brown, J. K. (1974), Handbook for inventorying downed woody material, *Gen. Tech. Rep. INT-16*, 24 pp., Intermountain For. and Range Exp. Stn., For. Serv., U. S. Dep. of Agric., Ogden, Utah.
- Burgan, R. E. (1988), 1988 Revisions to the 1978 National Fire-Danger Rating System, *Res. Pap. SE-273*, 39 pp., Southeastern For. Exp. Stn., For. Serv., U. S. Dep. of Agric., Asheville, N. C.
- Burns, R. M., and B. H. Honkala (1990), *Silvics of North America: 1. Conifers; 2. Hardwoods*, *Agric. Handbook*, 654, vol. 2, 877 pp., For. Serv., U. S. Dep. of Agric., Washington, D. C.
- Butler, B. W., J. Cohen, D. J. Latham, R. D. Schuette, P. Sopko, K. S. Shannon, D. Jimenez, and L. S. Bradshaw (2004), Measurements of radiant emissive power and temperatures in crown fires, *Can. J. For. Res.*, *34*, 1577–1587.
- Chen, L.-W. A., H. Moosmüller, W. P. Arnott, J. C. Chow, J. G. Watson, R. A. Susott, R. E. Babbitt, C. E. Wold, E. N. Lincoln, and W. M. Hao (2006), Particle emissions from laboratory combustion of wildland fuels: In situ optical and mass measurements, *Geophys. Res. Lett.*, *33*, L04803, doi:10.1029/2005GL024838.
- Christian, T. J., B. Kleiss, R. J. Yokelson, R. Holzinger, P. J. Crutzen, W. M. Hao, B. H. Saharjo, and D. E. Ward (2003), Comprehensive laboratory measurements of biomass-burning emissions: 1. Emissions from Indonesian, African, and other fuels, *J. Geophys. Res.*, *108*(D23), 4719, doi:10.1029/2003JD003704.
- Christian, T. J., B. Kleiss, R. J. Yokelson, R. Holzinger, P. J. Crutzen, W. M. Hao, T. Shirai, and D. R. Blake (2004), Comprehensive laboratory measurements of biomass-burning emissions: 2. First intercomparison of open-path FTIR, PTR-MS, GC-MS/FID/ECD, *J. Geophys. Res.*, *109*, D02311, doi:10.1029/2003JD003874.
- Crutzen, P. J., and M. O. Andreae (1990), Biomass burning in the tropics: Impact on atmospheric chemistry and biogeochemical cycles, *Science*, *250*, 1669–1678.

- Fons, W. L. (1946), Analysis of fire spread in light forest fires, *J. Agric. Res.*, 72, 93–121.
- Freeborn, P. H., B. L. Nordgren, W. M. Hao, R. H. Wakimoto, and L. P. Queen (2004), Ground-based thermal observations of the Black Mountain 2 Fire in west-central Montana, 2003, paper presented at Remote Sensing for Field Users: Tenth Forest Service Remote Sensing Applications Conference, For. Serv., U. S. Dep. of Agric., Salt Lake City, Utah, 5–9 Apr.
- Freeborn, P. H., C. C. Hardy, and B. W. Butler (2006), Coupling in-situ energy flux measurements of wildland fires with oblique thermal infrared imagery, paper presented at New Remote Sensing Technologies for Resource Managers: Eleventh Forest Service Remote Sensing Applications Conference, For. Serv., U. S. Dep. of Agric., Salt Lake City, Utah, 24–28 Apr.
- Fuss, S. P., and A. Hamins (2002), An estimate of the correction applied to radiant flame measurements due to attenuation by atmospheric CO₂ and H₂O, *Fire Safety J.*, 37, 181–190.
- Goode, J. G., R. J. Yokelson, R. A. Susott, and D. E. Ward (1999), Trace gas emissions from laboratory biomass fires measured by open-path Fourier transform infrared spectroscopy: Fires in grass and surface fuels, *J. Geophys. Res.*, 104(D17), 21,237–21,245.
- Hao, W. M., and M. H. Liu (1994), Spatial and temporal distribution of tropical biomass burning, *Global Biogeochem. Cycles*, 8(4), 495–503.
- Hao, W. M., M. H. Liu, and P. J. Crutzen (1990), Estimates of annual and regional releases of CO₂ and other trace gases to the atmosphere from fires in the tropics, based on the FAO statistics for the period 1975–1980, in *Fire in the Tropical Biota: Ecosystem Processes and Global Challenges*, *Ecol. Stud.*, vol. 84, pp. 440–462, edited by J. G. Goldammer, Springer, Berlin.
- Hao, W. M., D. E. Ward, G. Olbu, and S. P. Baker (1996), Emissions of CO₂, CO, and hydrocarbons from fires in diverse African savanna ecosystems, *J. Geophys. Res.*, 101(D19), 23,577–23,584.
- Ichoku, C., and Y. J. Kaufman (2005), A method to derive smoke emission rates from MODIS fire radiative energy measurements, *IEEE Trans. Geosci. Remote Sens.*, 43(11), 2636–2649.
- Kaufman, Y. J., C. J. Tucker, and I. Fung (1990), Remote sensing of biomass burning in the tropics, *J. Geophys. Res.*, 95(D7), 9927–9939.
- Kaufman, Y. J., L. A. Remer, R. D. Ottmar, D. E. Ward, R. R. Li, R. Kleidman, R. S. Fraser, L. P. Flynn, D. McDougal, and G. Shelton (1996), Relationship between remotely sensed fire intensity and rate of emission of smoke: SCAR-C Experiment, in *Global Biomass Burning*, edited by J. Levine, pp. 685–696, MIT Press, Cambridge, Mass.
- Kaufman, Y. J., C. O. Justice, L. P. Flynn, J. D. Kendall, E. M. Prins, L. Giglio, D. E. Ward, W. P. Menzel, and A. W. Setzer (1998), Potential global fire monitoring from EOS-MODIS, *J. Geophys. Res.*, 103(D24), 32,215–32,338.
- Klass, D. L. (1998), *Biomass for Renewable Energy, Fuels, and Chemicals*, 394 pp., Academic Press, San Diego, Calif.
- Lobert, J. M., D. H. Scharffe, W. M. Hao, T. A. Kuhlbusch, R. Seuwen, P. Warneck, and P. J. Crutzen (1991), Experimental evaluation of biomass burning emissions: Nitrogen and carbon containing compounds, in *Global Biomass Burning: Atmospheric, Climatic, and Biospheric Implications*, edited by J. S. Levine, pp. 289–304, MIT Press, Cambridge, Mass.
- McCarter, R. J., and A. Broide (1965), Radiative and convective energy from wood crib fires, *Pyrodynamics*, 2, 65–85.
- Nelson, R. M. (1982), An evaluation of the carbon mass balance technique for estimating emission factors and fuel consumption, *Res. Pap. SE-231*, 9 pp., Southeastern For. Exp. Stn., For. Ser., U. S. Dep. of Agric., Asheville, N. C.
- Roberts, G., M. J. Wooster, G. L. W. Perry, N. Drake, L.-M. Rebelo, and F. Dipotso (2005), Retrieval of biomass combustion rates and totals from fire radiative power observations: Application to southern Africa using geostationary SEVIRI imagery, *J. Geophys. Res.*, 110, D21111, doi:10.1029/2005JD006018.
- Sandberg, D. V. (1974), Slash fire intensity and smoke emissions, paper presented at Third National Conference on Fire and Forest Meteorology, Am. Meteorol. Soc., Lake Tahoe, Calif., 2–4 Apr.
- Scholes, R. J., J. Kendall, and C. O. Justice (1996a), The quantity of biomass burned in southern Africa, *J. Geophys. Res.*, 101(D19), 23,667–23,676.
- Scholes, R. J., D. E. Ward, and C. O. Justice (1996b), Emissions of trace gases and aerosol particles due to vegetation burning in southern hemisphere Africa, *J. Geophys. Res.*, 101(D19), 23,677–23,682.
- Seiler, W., and P. J. Crutzen (1980), Estimates of gross and net fluxes of carbon between the biosphere and atmosphere from biomass burning, *Clim. Change*, 2, 207–247.
- Susott, R. A. (1982a), Characterization of the thermal properties of forest fuels by combustible gas analysis, *For. Sci.*, 28(2), 404–420.
- Susott, R. A. (1982b), Differential scanning calorimetry of forest fuels, *For. Sci.*, 28(4), 839–851.
- Susott, R. A., W. F. DeGroot, and F. Shafizadeh (1975), Heat content of natural fuels, *J. Fire Flammability*, 6, 311–325.
- Susott, R. A., F. Shafizadeh, and T. W. Aanerud (1979), A quantitative thermal analysis technique for combustible gas detection, *J. Fire Flammability*, 10, 94–104.
- Susott, R. A., D. E. Ward, R. E. Babbitt, D. J. Latham, L. G. Weger, and P. M. Boyd (1990), Fire dynamics and chemistry of large fires, final report, 39 pp., Fire Chem. Res. Work Unit, Intermountain Res. Stn., For. Serv., U. S. Dep. of Agric., Missoula, Mont.
- Taylor, J. A., and P. R. Zimmerman (1991), Modeling trace gas emissions from biomass burning, in *Global Biomass Burning: Atmospheric, Climatic and Biospheric Implications*, edited by J. S. Levine, pp. 345–350, MIT Press, Cambridge, Mass.
- Ward, D. E., and C. C. Hardy (1991), Smoke emissions from wildland fires, *Environ. Int.*, 17, 117–134.
- Ward, D. E., and L. F. Radke (1993), Emissions measurements from vegetative fires: a comparative evaluation of methods and results, in *Fire in the Environment: The Ecological Atmospheric, and Climatic Importance of Vegetation Fires*, edited by P. J. Crutzen and J. G. Goldammer, pp. 53–76, John Wiley, Chichester, U.K.
- White, R. H., and M. A. Dietenberger (1999), Fire safety, in *Wood Handbook—Wood as an Engineering Material, Gen. Tech. Rep. FPL-GTR-113*, chap. 17, For. Prod. Lab., For. Serv., U. S. Dep. of Agric., Madison, Wis.
- Wooster, M. J. (2002), Small-scale experimental testing of fire radiative energy for quantifying mass combusted in natural vegetation fires, *Geophys. Res. Lett.*, 29(21), 2027, doi:10.1029/2002GL015487.
- Wooster, M. J., and Y.-H. Zhang (2004), Boreal forest fires burn less intensely in Russia than in North America, *Geophys. Res. Lett.*, 31, L20505, doi:10.1029/2004GL020805.
- Wooster, M. J., B. Zhukov, and D. Oertel (2003), Fire radiative energy for quantitative study of biomass burning from the BIRD experimental satellite and comparison to MODIS fire products, *Remote Sens. Environ.*, 86, 83–107.
- Wooster, M. J., G. Perry, B. Zhukov, and D. Oertel (2004), Biomass burning emissions inventories: Modelling and remote sensing of fire intensity and biomass combustion rates, in *Spatial Modelling of the Terrestrial Environment*, edited by R. Kelly, N. Drake, and S. Barr, pp. 175–196, John Wiley, Hoboken, N. J.
- Wooster, M. J., G. Roberts, G. L. W. Perry, and Y. J. Kaufman (2005), Retrieval of biomass combustion rates and totals from fire radiative power observations: FRP derivation and calibration relationships between biomass consumption and fire radiative energy release, *J. Geophys. Res.*, 110, D24311, doi:10.1029/2005JD006318.
- Yokelson, R. J., D. W. T. Griffith, and D. E. Ward (1996), Open-path Fourier transform infrared studies of large-scale laboratory biomass fires, *J. Geophys. Res.*, 101(D15), 21,067–21,080.

S. P. Baker, W. M. Hao, B. L. Nordgren, and C. A. Ryan Fire Sciences Laboratory, Rocky Mountain Research Station, U.S. Forest Service, Missoula, MT 59808, USA.

P. H. Freeborn and M. J. Wooster, Department of Geography, King's College London, London WC2R 2LS, UK. (patrick.freeborn@kcl.ac.uk)

C. Ichoku, Earth Science System Interdisciplinary Center, University of Maryland, College Park, MD 20742, USA.